Pergamon

0045-7949(94)00365-3

Computers & Structures Vol. 54, No. 4, pp. 655–670, 1995
Copyright © 1995 Elsevier Science Ltd
Printed in Great Britain. All rights reserved
0045-7949/95 $9.50 + 0.00

DEEP PENETRATION OF THICK THERMOVISCOPLASTIC TARGETS BY LONG RIGID RODS

Xingju Chen and **R. C. Batra**†

Department of Mechanical and Aerospace Engineering and Engineering Mechanics,
University of Missouri–Rolla, Rolla, MO 65401-0249, U.S.A.

(*Received* 7 *August* 1993)

Abstract—We analyze axisymmetric thermomechanical deformations of a thick thermoviscoplastic target being penetrated by a fast-moving rigid cylindrical hemispherical-nosed penetrator. The target material is assumed to exhibit strain and strain-rate hardening and thermal softening. The target/penetrator interface is assumed to be smooth. In the solution of the problem by the finite element method, the mesh is refined automatically whenever one of its elements has been severely distorted, such that a very fine mesh is generated in the region adjoining the target/penetrator interface and the mesh size increases gradually as one moves away from this interface. The computed depth of penetration has been found to correlate well with the test values. We also give details of the deformation fields, such as the history of the temperature at a material point, contours of the pressure field and the distribution of the velocity field in the deforming region.

1. INTRODUCTION

Factors that play a significant role during the penetration of metal targets by projectiles include material properties, impact velocity, projectile shape, target support position and relative dimensions of the target and the projectile. Here we consider kinetic energy penetrators, which for terminal ballistic purposes may be considered as long metal rods traveling at high speeds. At ordnance speeds in the range of 0.5–2 km/sec, material strength becomes an important parameter. Engineering models proposed by Allen and Rogers [1], Pack and Evans [2], Alekseevskii [3] and Tate [4, 5] account for material strength by including these as resistive pressures in the Bernoulli equation. These resistive pressures are empirically determined quantities and the predicted results depend strongly upon the assumed values of these pressures. Wright and Frank [6] have re-examined Tate's theory and derived expressions for the resistive pressures in terms of mass densities, yield strengths of the penetrator and target materials, and penetrator speed.

Backman and Goldsmith [7] have reviewed the open literature on ballistic penetration from the 1800s to 1977 and have cited 278 references. They describe different physical mechanisms involved in the penetration and perforation processes and also discuss a number of engineering models. Other review papers include those by Jonas and Zukas [8] and Anderson and Bodner [9]. Three books [10–12], published during the past few years, provide extensive discussions of engineering models, experimental techniques, analytical models and numerical simulation of perforation.

Here we study the thermomechanical deformations of a thick target being penetrated by a fast moving hemispherical-nosed cylindrical rod made of a material considerably stronger than that of the target, so that the penetrator can be regarded as being rigid. For example, Forrestal *et al.* [13] observed that during their penetration tests involving steel rods and aluminum targets, the penetrator remained virtually undeformed. One of our objectives is to simulate these tests and provide details of deformations of the target. Another objective is to decipher regions of severe localization of the deformation. Since the width of these regions is controlled by, among other factors, the thermal conductivity, it is necessary to include the effects of heat conduction in the problem. Nearly all of the commercially available codes (e.g. see [10]) neglect the effect of heat conduction and regard the temperature within an element to be uniform. When the deforming region is rezoned and values of temperature, etc. are computed at the newly created nodes, excessive diffusion out of the computed temperature field results, since temperatures at the element centroids are originally computed in the code. These problems have been alleviated in the code developed to analyze the present problem, since we include the effects of heat conduction and regard temperature as a field variable and compute its values at the node points. Also, the code uses an algorithm developed by Batra and Ko [24] to refine the mesh whenever an interior angle of a triangular element becomes less than 15°, or the ratio of its altitude to the base is less than 0.12. The newly generated mesh

---

† Present address: Clifton Garvin Professor, Department of Engineering Science and Mechanics, Virginia Polytechnic Institute and State University, Blacksburg, VA 24061-0219, U.S.A.

is very fine near the target/penetrator interface, where severe deformations of the target occur, and gradually becomes coarser as one moves away from it. The size of the largest and the smallest element can be controlled by adjusting the input variables. We employ the full integration rule and do not include artificial viscosity.

The computed depth of penetration for the 16 tests described by Forrestal *et al.* [13] has been found to match well with that determined experimentally. Also, the temperature of target particles adjacent to the target/penetrator interface was close to the melting temperature of the material, which at least partially explains the microstructural changes reported by Forrestal *et al.* in a thin layer of the target material adjoining the tunnel surface. The computed depth of penetration decreases with an increase in the values of the strain-hardening and strain-rate hardening exponents.

2. FORMULATION OF THE PROBLEM

We study a penetration problem in which a rigid cylindrical hemispherical-nosed penetrator impacts a deformable target at normal incidence and assume that the deformations of the target are axisymmetric. We use a fixed set of cylindrical coordinates with the z-axis coincident with the axis of symmetry of deformations and pointing into the target and the origin at the top surface of the undeformed target. In the referential description, equations governing the thermomechanical deformations of the target are

$$(\rho J)^{\boldsymbol{\cdot}} = 0, \tag{1}$$

$$\rho_0 \dot{\mathbf{v}} = \mathrm{Div}\,\mathbf{T}, \tag{2}$$

$$\rho_0 \dot{e} = -\mathrm{Div}\,\mathbf{Q} + tr(\mathbf{T}\dot{\mathbf{F}}^T), \tag{3}$$

where

$$J = \det \mathbf{F}, \quad \mathbf{F} = \mathrm{Grad}\,\mathbf{x}, \tag{4}$$

$\mathbf{x}$ is the present position of a material particle that occupied place $\mathbf{X}$ in the reference configuration, ρ its present mass density, ρ_0 its mass density in the reference configuration, $\mathbf{v}$ the present velocity of a material particle, $\mathbf{T}$ the first Piola–Kirchhoff stress tensor, e the specific internal energy, $\mathbf{Q}$ the heat flux per unit reference area, a superimposed dot indicates the material time derivative and operators Grad and Div signify the gradient and divergence of field quantities defined in the reference configuration. The balance laws (1)–(3) are supplemented by the following constitutive relations.

$$\boldsymbol{\sigma} = -p(\rho)\mathbf{1} + 2\mu\mathbf{D} \tag{5}$$

$$\mathbf{T} = \frac{\rho_0}{\rho}\boldsymbol{\sigma}(\mathbf{F}^{-1})^T \tag{6}$$

$$2\mu = \frac{\sigma_0}{\sqrt{3}I}\left(\frac{\psi}{\psi_0}\right)^n (1 + bI)^m (1 - \nu\theta) \tag{7}$$

$$2\mathbf{D} = \mathrm{grad}\,\mathbf{v} + (\mathrm{grad}\,\mathbf{v})^T \tag{8}$$

$$\bar{\mathbf{D}} = \mathbf{D} - \tfrac{1}{3}(tr\mathbf{D})\mathbf{1} \tag{9}$$

$$2I^2 = tr(\bar{\mathbf{D}}^2) \tag{10}$$

$$p = p_{\mathrm{H}}\left(1 - \frac{\Gamma\mu}{2}\right) + \Gamma\rho(e - e_0) \tag{11}$$

$$p_{\mathrm{H}} = \frac{\rho_0 c_0^2 \eta}{(1 - s\eta)^2} \tag{12}$$

$$\eta = 1 - \frac{\rho_0}{\rho} \tag{13}$$

$$\mu = \frac{\rho}{\rho_0} - 1 \tag{14}$$

$$\mathbf{Q} = -k\frac{\rho_0}{\rho}\,\mathrm{grad}\,\theta(\mathbf{F}^{-1})^T \tag{15}$$

$$\dot{e} = c\dot{\theta} + \dot{\rho}p(\rho)/\rho^2 \tag{16}$$

$$\dot{\psi} = \frac{tr(\boldsymbol{\sigma}\bar{\mathbf{D}})}{\sigma_0\left(\frac{\psi}{\psi_0}\right)^n}. \tag{17}$$

Here $\boldsymbol{\sigma}$ is the Cauchy stress tensor, σ_0 the yield stress of the target material in a quasistatic simple tension or compression test, ψ_0 the strain at yield, n the strain-hardening exponent, ν the coefficient of thermal softening, θ the temperature rise of a material particle, ρ the present mass density of a material particle whose mass density in the reference configuration is ρ_0, e is the specific internal energy, k the thermal conductivity and c the specific heat. The internal variable ψ may be associated with an equivalent plastic strain; its evolution is given by eqn (17). Equation (11) is the Mie–Gruniesen equation of state.

Batra and Jayachandran [14] used three constitutive relations, namely, (5) with $(\psi/\psi_0)^n$ in eqns (7) and (17) replaced by $(1 + \psi/\psi_0)^n$, the Bodner–Partom flow rule [15] and that proposed by Brown, Kim and Anand [16]. They calibrated the three flow rules against a hypothetical simple compression test performed at a nominal strain-rate of $3300\,\mathrm{sec}^{-1}$ and found that each predicted essentially identical response of the target being deformed by a fast-moving rigid hemispherical-nosed penetrator. We note that these three constitutive relations model the effect of strain-hardening, strain-rate hardening and thermal softening in different ways. Thus the macroscopic effects of deformation seem less sensitive to the way in which strain-hardening, strain-rate hardening and thermal softening are modeled in the constitutive relation.

Since the hemispherical-nosed penetrator is being modeled as a rigid body and its motion is along the z-axis, its equation of motion can be written as

$$M\dot{v}_z = -2\pi r_0^2 \int \mathbf{n}\cdot\boldsymbol{\sigma}\mathbf{n}\sin 2\phi \, \mathrm{d}\phi, \qquad (18)$$

where $\mathbf{n}$ is an outward unit normal at a point on the target surface abutting the penetrator nose, M is the mass of the penetrator, r_0 its radius and ϕ is the angular position, measured counter-clockwise from the vertical centroidal axis, of a point on the penetrator nose. The rigid motion of the penetrator and the deformations of the target are coupled through eqn (18) and the boundary conditions at the common interface between the two. Recalling that the target/penetrator interface is taken to be smooth, the penetrator experiences the resistance force because of normal tractions acting on its hemispherical nose. Thus, the integration in eqn (18) is only for those values of ϕ between 0 and $\pi/2$ for which points on the nose surface are in contact with the deforming target region.

For the finite target region ABCDEFA, shown in Fig. 1, we impose the following boundary conditions:

$$\boldsymbol{\sigma}\mathbf{n} = \mathbf{0}, \qquad (19)$$

$$\mathbf{q}\cdot\mathbf{n} = h(\theta - \theta_a) \qquad (20)$$

on FED,

$$\sigma_{rz} = 0, \qquad (21)$$

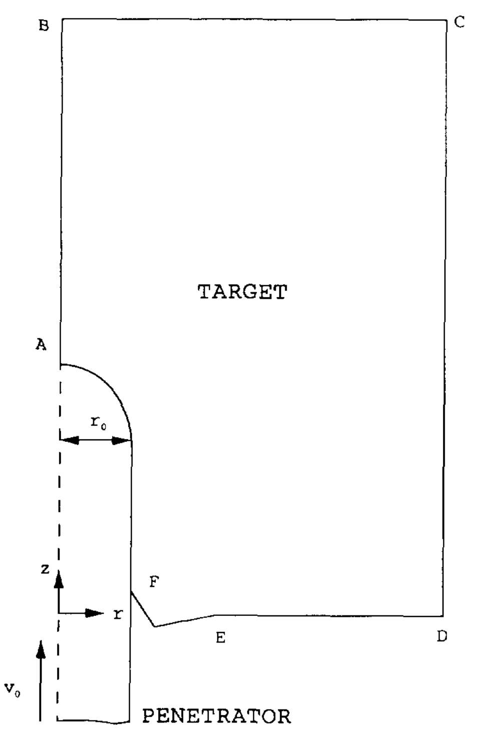

Fig. 1. A schematic sketch of the problem studied.

$$v_r = 0, \qquad (22)$$

$$q_r = 0, \qquad (23)$$

on the axis of symmetry AB,

$$\mathbf{q}\cdot\mathbf{n} = 0, \qquad (24)$$

$$\boldsymbol{\sigma}\mathbf{n} = 0 \qquad (25)$$

at a point on AF where the penetrator surface is not in contact with the deforming target region,

$$\mathbf{q}\cdot\mathbf{n} = 0, \qquad (26)$$

$$[\mathbf{v}\cdot\mathbf{n}] = 0, \qquad (27)$$

$$\mathbf{e}\cdot\boldsymbol{\sigma}\mathbf{n} = 0 \qquad (28)$$

at points on AF where the penetrator and target surfaces are in contact with each other and

$$\boldsymbol{\sigma}\mathbf{n} = 0, \qquad (29)$$

$$\mathbf{q}\mathbf{n} = 0 \qquad (30)$$

on the bounding surfaces BC and CD.
Here $\mathbf{q}$ is the heat flux measured per unit area in the present configuration, θ_a is the room temperature, h the heat transfer coefficient between the target material and the air, $[f]$ in (27) indicates the jump of f across the target/penetrator interface and $\mathbf{e}$ is a unit vector tangent to the target/penetrator interface. Boundary conditions (21)–(23) follow from the presumed symmetry of deformations, (27) states that there is no inter-penetration of the target material into the penetrator and vice versa, and (28) is equivalent to the statement that the target/penetrator interface is smooth. The boundary conditions (29) and (30) are justified, since these surfaces are far away from the penetrator/target interface.

We assume that the target is initially at rest, is stress-free, has a uniform mass density ρ_0 and a uniform temperature θ_a. The initial velocity of the rigid penetrator is v_0 in the positive z-direction and, at time $t = 0$, it just impacts the top surface of the target at normal incidence.

The problem formulated above is highly nonlinear and too complicated to solve analytically. Therefore, we seek its approximate solution by the finite element method.

3. COMMENTS ON COMPUTATIONAL ASPECTS OF THE PROBLEM

Substitution for $\mathbf{T}$, $\mathbf{Q}$ and e from eqns (5)–(17) into eqns (1)–(4) results in coupled nonlinear partial differential equations which, with prescribed initial conditions and boundary conditions, are to be solved for ρ, $\mathbf{v}$, ψ and θ. One also needs to account for the interaction between the rigid penetrator and the deformable target. We use the updated Lagrangian formulation [17] of the problem to get its approximate solution. That is, in order to find the fields of ρ, $\mathbf{v}$ and θ in the body at time $t + \Delta t$, the configuration of the body at time t is taken as the reference configuration. The governing nonlinear partial differential equations are first reduced to a set of coupled nonlinear ordinary differential equations by using the Galerkin approximation [17], the lumped mass matrix obtained by the row–sum technique and three quadrature points are used to numerically integrate various quantities over an element. These equations are integrated with respect to time t by using the forward difference method, which for linear problems is explicit and conditionally stable. Since we have considered only volumetric elastic strains, the bulk wave speed is used to compute the time step size. Additional restrictions on it are imposed by the slide line algorithm used to account for the contact conditions at the target/penetrator interface.

After every time increment, the coordinates of node points are updated and elements in the finite element mesh are checked for excessive distortion. If either one of the interior angles of a triangular element is less than 15°, or the ratio of its altitude to the base is less than 0.12, then the element is considered to have been severely distorted, and the mesh is refined so that finer elements are generated in the region adjoining the target/penetrator interface and the element size increases gradually as one moves away from this surface. Additional restrictions imposed on the element size when generating the new mesh are that an altitude of any triangular element will not be less than $0.25r_0$ or greater than r_0, where r_0 equals the radius of the cylindrical part of the penetrator. The values of the nodal variables at the newly generated nodes are obtained by first determining to which element in the old mesh the node belongs and then by interpolating from the values at the nodes of that element.

The mechanical boundary conditions (25), (27) and (28) on the target/penetrator interface AF in Fig. 1 are accounted for by using the slide line algorithm described by Hallquist *et al.* [18]. We regard the rigid penetrator surface as the master surface and the adjoining surface of the deformable target as the slave surface, naming nodes on it and elements sharing at least one side with the penetrator surface as slave nodes and slave elements, respectively. After each time increment, we find the normal acceleration of each slave node relative to the master surface. If this relative normal acceleration points away from the master surface, the node is released and is assumed not to be in contact with the master surface during the next time step. However, if the relative normal acceleration of a slave node is towards the master surface and its distance from the master surface is less than a preassigned small number, the slave node is taken to be on the master surface during the subsequent computations.

4. NUMERICAL RESULTS AND DISCUSSION

We have developed a computer code based on the above stated formulation of the problem, and used it to simulate the penetration tests described by Forrestal *et al.* [13]. They also gave the stress–strain curve for the 6061-T651 aluminum target material deformed essentially quasistatically in simple compression. At high strain rates, that are likely to occur at points adjoining the target/penetrator interface, most metals exhibit strain-rate hardening and thermal softening [19]. Here we take the following values of material parameters.

$$\begin{aligned}
&\sigma_0 = 276\ \text{MPa}, \quad n = 0.051, \quad \psi_0 = 0.004,\\
&b = 10{,}000\ \text{sec}, \quad m = 0.01,\\
&\nu = 0.00153/^\circ\text{C}, \quad \rho_0 = 2710\ \text{kg/m}^3,\\
&c_0 = 5041\ \text{m/s}, \quad s = 1.420, \quad \Gamma = 2.0,\\
&k = 120\ \text{W/m}/^\circ\text{C}, \quad c = 875\ \text{J/kg}/^\circ\text{C},\\
&\theta_a = 22^\circ\text{C}, \quad h = 20\ \text{W/m}^2/^\circ\text{C}.
\end{aligned} \tag{31}$$

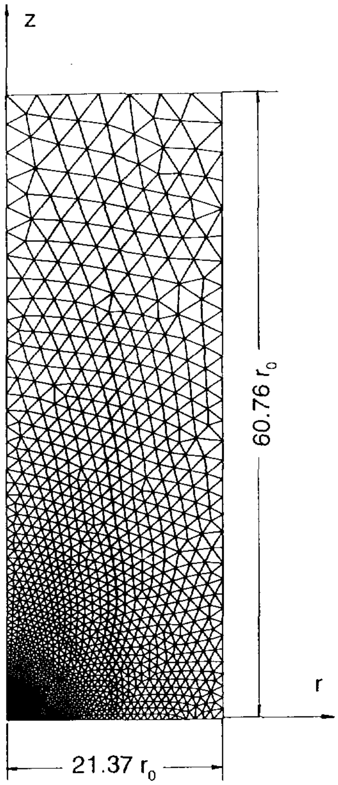

Fig. 2. A typical finite target region analyzed and its discretization into finite elements.

For these values of material parameters, the stress–strain curve in a quasistatic compression test mimics well that given by Forrestal *et al.* [13] for aluminum. Here we also study the effect of different values of m and n on the penetration process.

In the ballistic experiments of Forrestal *et al.* [13], a 20 mm smooth-bore powder gun launched T-200 maraging steel hemispherical nosed cylindrical rods, impacting 6061-T651 aluminum targets at normal incidence. They observed that the major penetration mechanism was ductile hole growth and their post-test observations revealed that penetrators remained essentially undeformed. Thus, it is reasonable to regard the penetrator as a rigid body and our model should simulate their tests well.

Preliminary computations for a few test conditions indicated that a thin layer of the target material adjoining the target/penetrator interface melted before the penetration process was completed. According to our constitutive hypotheses (5) and (7), when $\theta = 1/v$ = melting temperature of the material, $\mu = 0$ and the material behaves like an ideal fluid and cannot support any shear stresses. Thus, it can undergo unlimited shearing deformations with the application of very little shearing force and the finite element mesh in a small region abutting the target/penetrator interface will get severely distorted

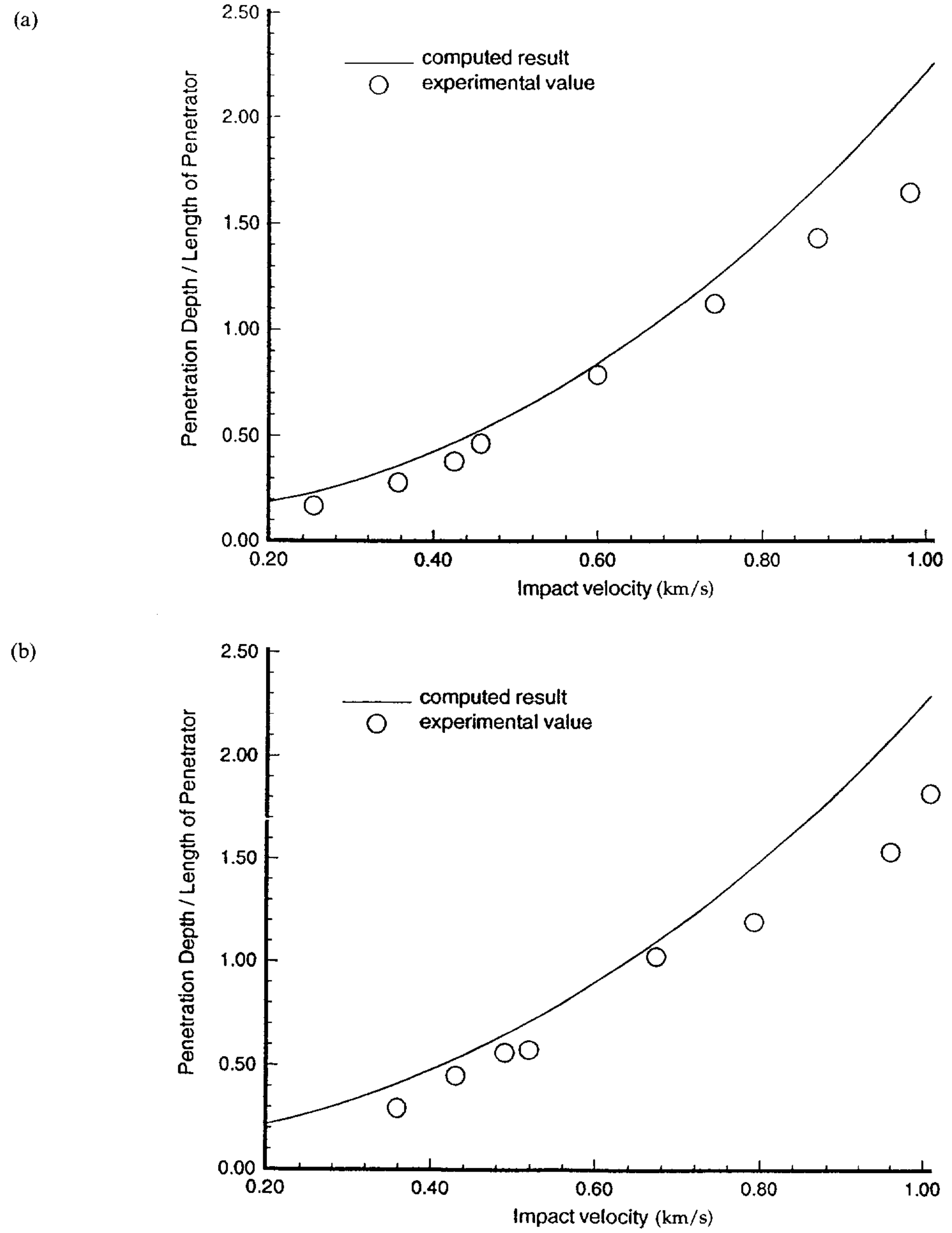

Fig. 3. Normalized penetration depth vs the impact speed. (a) Penetrator radius $r_0 = 2.54$ mm. (b) Penetrator radius $r_0 = 3.555$ mm.

in virtually no time. To alleviate this problem, for $\theta > 0.955\theta_m$, eqn (7) was modified to:

$$2\mu = \frac{0.045}{\sqrt{3}I}\left(\frac{\psi}{\psi_0}\right)^n (1 + bI)^m, \tag{32}$$

where θ_m is the melting temperature of the target material. We note that previous numerical simulations of similar tests, involving conical-nosed penetrators by Chen [20] and the engineering model proposed by Forrestal *et al.* [13], do not consider the thermal softening of the material.

Figure 2 shows the target region for one of the tests conducted by Forrestal *et al.*; its initial discretization into finite elements is also depicted. The initial mesh consisted of 2810 three-noded triangular elements and had 1488 nodes; for other domains the number of elements and nodes was suitably changed. During the course of computations, the mesh was refined so as to concentrate fine elements within the intensely deforming region and coarse elements elsewhere. Thus, the number of nodes and elements in the mesh kept on changing with time.

Figure 3 provides a comparison of the computed depth of penetration with that found experimentally for two different penetrator radii of 2.54 mm and 3.555 mm. The curves depict the computed penetration depth normalized by the penetrator length vs the impact speed and reveal that the computed penetration depth matches well with that found experimentally for low impact speeds, but the two differ

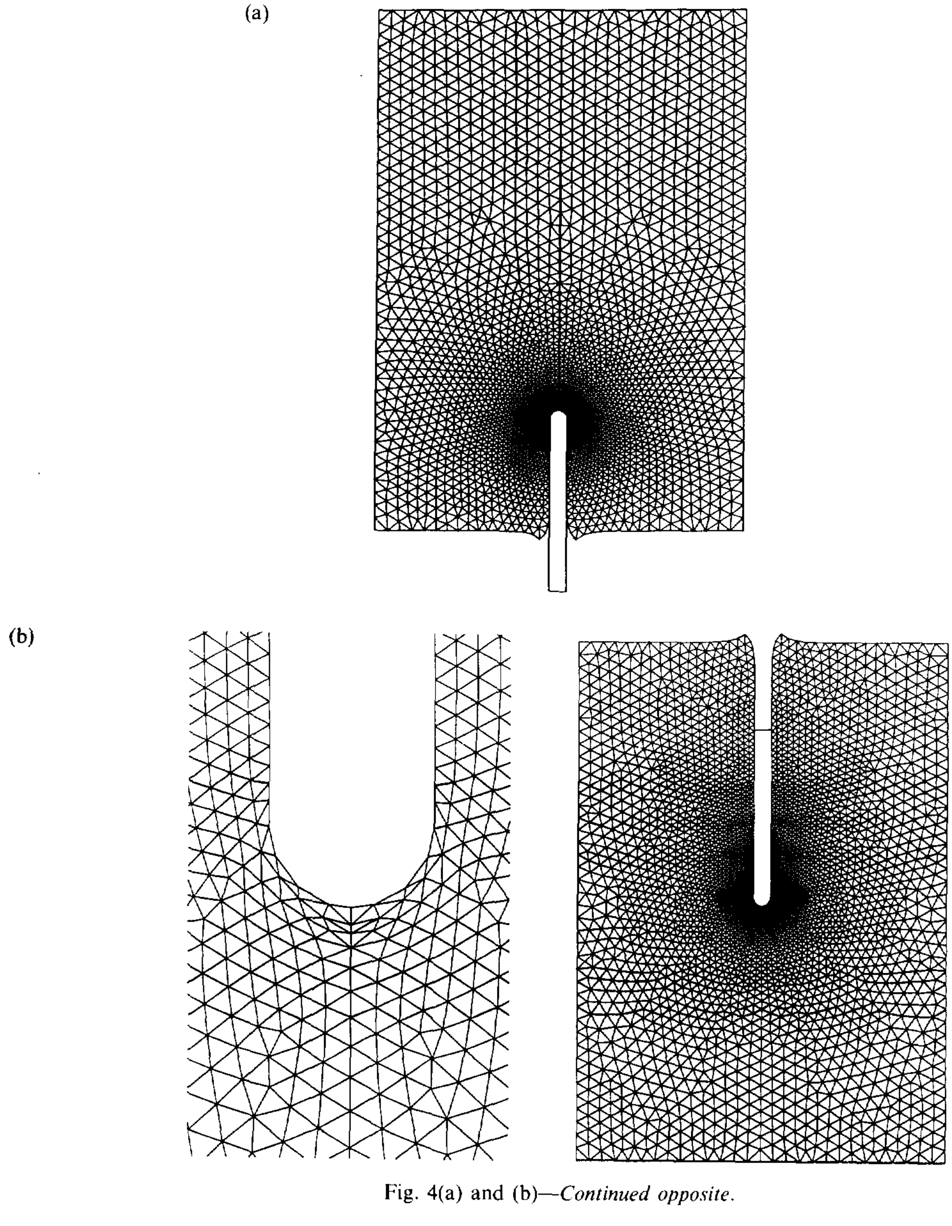

Fig. 4(a) and (b)—*Continued opposite.*

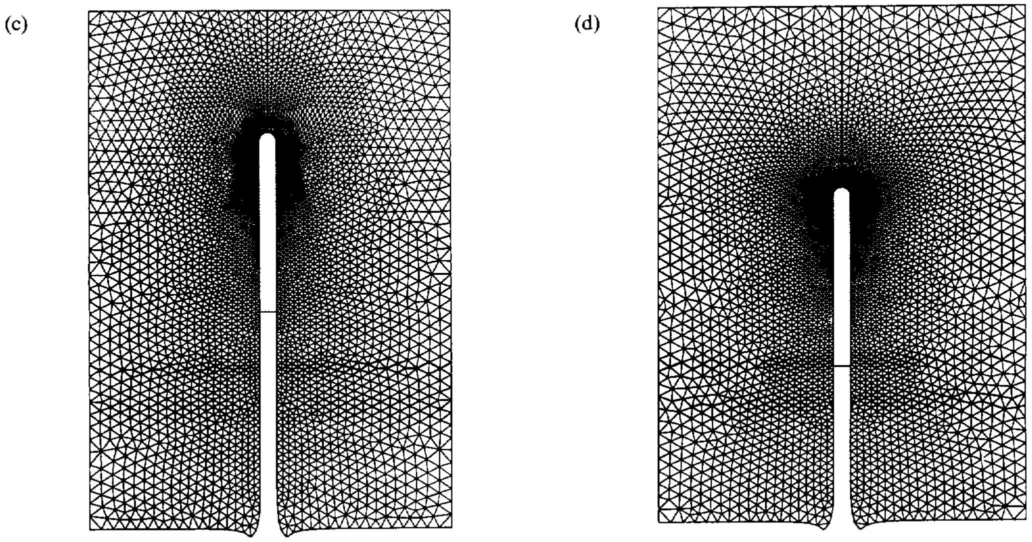

Fig. 4. Tunnel shapes when the penetrator speed has been reduced to 0.854, 0.583, 0.395 and 0.002 times the initial impact speed of 1.009 km/s.

for higher values of the impact speed. Some of the reasons for this discrepancy are:

(i) frictional force at the target/penetrator interface;
(ii) dependence of material properties of the target upon the temperature rise;
(iii) blunting of the penetrator nose at higher impact speeds;
(iv) smoothing out of the computed fields after every mesh refinement; and
(v) support conditions at the back surface of the target.

Precautions were taken to minimize the last effect. Also, dynamic effects such as recovery and recrystallization have been neglected.

We note that the test data for the range of temperatures, strains and strain-rates encountered in a typical penetration process is not available in the open literature. In the tests and hence in our simulations, the target length equalled four to five times the penetration depth for low impact speeds and only twice the penetration depth for higher speeds. Thus, support conditions at the back surface may affect more the penetration depth at high impact speeds than at low speeds. We took the back surface to be traction-free in every case.

Chen [20] numerically simulated the perforation and penetration tests of Forrestal *et al.* [21] involving conical-nosed penetrators by using the Lagrangian computer code PRONTO2D. He assumed the existence of a tiny hole along the axis of symmetry, modeled the target material as elastic linearly strain hardening, presumed Coulomb's friction with a constant coefficient of friction and assigned to it the value 0.1. His computed depth of penetration matched well with that found experimentally for low speeds of impact, but was lower than the test value for higher impact speeds. A reason for his under-predicting the penetration depth and our over-predicting it for high impact speeds is that we account for thermal softening of the material and he does not. The softening of the target material reduces the resistance it offers to the penetrator and thus results in penetration depth larger than that which would be obtained if the material did not thermally soften. At low impact speeds, the rise in temperature of the target material is small and does not significantly affect the penetration depth. Chen's consideration of frictional force at the target/penetrator interface should somewhat reduce the computed depth of penetration. Neither we nor Chen [20] incorporated any failure criterion into the problem formulation. However, our assumption that the material strength becomes minuscule once its temperature has risen to 95.5% of the

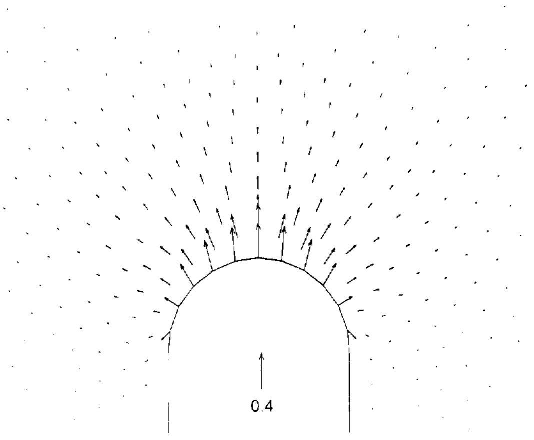

Fig. 5. Velocity distribution in the deforming target region when the penetrator speed equals 0.395 times its striking speed.

melting temperature [cf. eqn. (32)] tacitly accounts for the failure of the material.

The geometry of the tunnel produced in the target when the penetrator of radius 3.555 mm and mass 23.32 g impacts the target at normal incidence at a speed of 1.009 km/sec is shown in Fig. 4(a)–(d) at four instants of the penetration process. The finite element meshes being used to analyze the target deformations at these instants are also shown in these figures; a blow-up of the mesh around the penetrator nose for the configuration of Fig. 4(b) indicates the relative size of elements in the dark regions of the figures. We note that the tunnel shape near the entrance region stays unaltered during the time the penetrator speed decreases from 0.854 to 0.002 times the initial striking speed. A close examination of the values of the second invariant of the deviatoric strain-rate tensor at the element centroids reveals that the target material within, at most, two penetrator diameters of the penetrator nose and one penetrator radius of the remaining target/penetrator interface is deforming severely. Computed results at other instants of the penetration process indicate that the size of the severely deforming target region ahead of the penetrator nose increases with time, until the penetrator speed has decreased to approximately 0.44

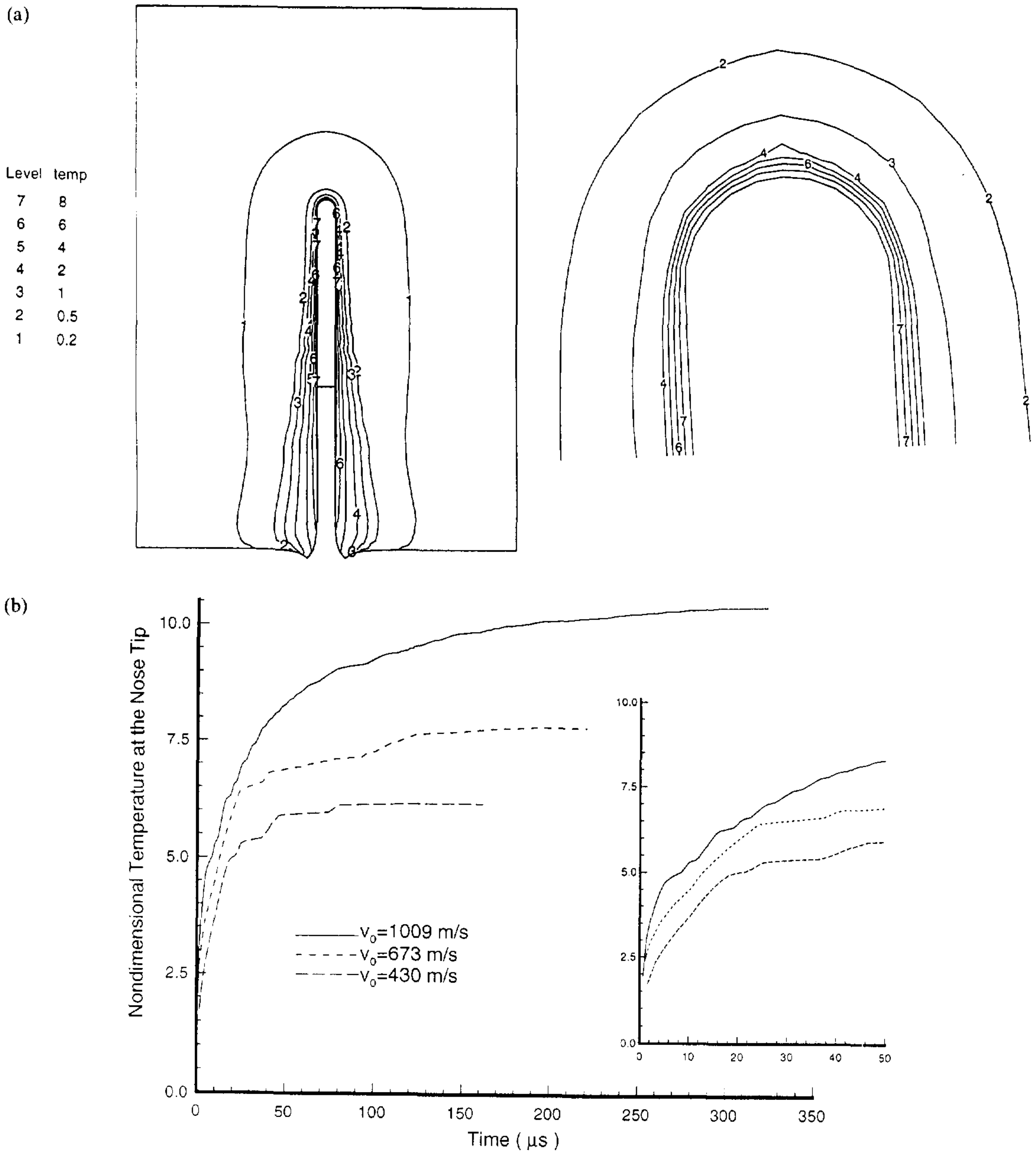

Fig. 6. (a) Contours of the nondimensional temperature rise in the deforming target region when the penetrator speed has been reduced to 43.54% of its initial value of 1.009 km/sec. (b) History of the evolution of the temperature rise at the stagnation point for three different impact speeds.

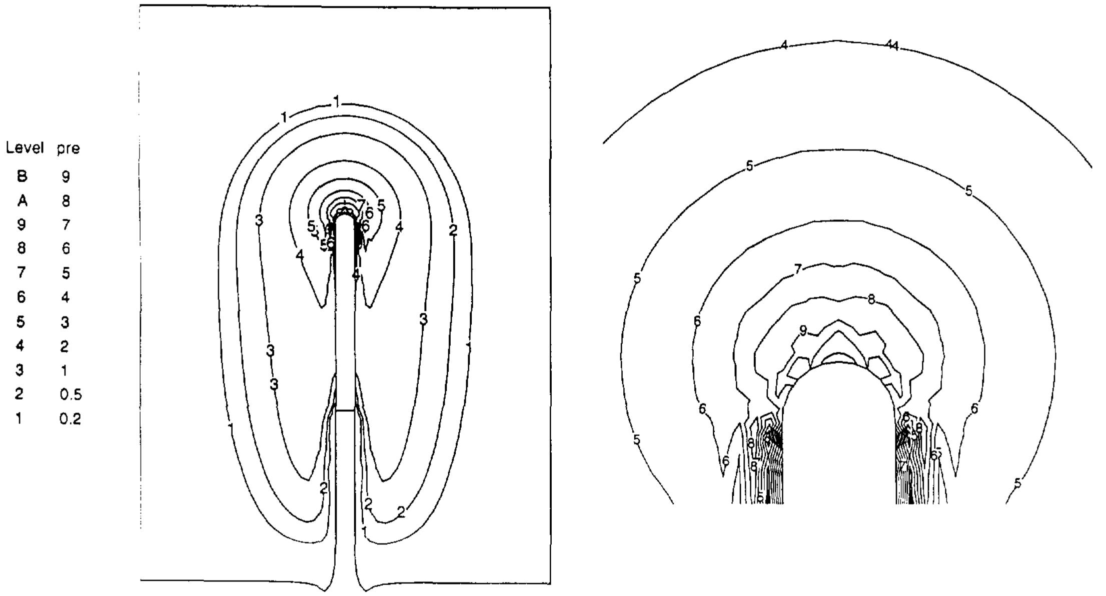

Fig. 7. Contours of the nondimensional hydrostatic pressure in the deforming target region when the penetrator speed equals 39.5% of its initial value.

times the initial impact speed, and subsequently decreases and becomes minuscule at a penetrator speed of 0.003 times its initial speed.

The velocity of target particles when the penetrator speed has been reduced to 39.5% of its striking speed is shown in Fig. 5. It is clear that the speed of target particles decreases sharply as one moves away from the target/penetrator interface. Target particles ahead of the penetrator nose have higher speeds than those near its lateral surfaces.

In Fig. 6(a) we have plotted contours of the temperature rise θ in the deforming target region when the penetrator has been slowed down to 39.5% of its initial impact speed. The temperature rise at a material point is indicative of its accumulated plastic deformation. The nondimensional temperature is to be multiplied by 116.4°C to obtain the corresponding dimensional value. These temperature contours suggest that the temperature of target particles adjoining the target/penetrator interface has become close to the melting temperature of the material and only the aforestated thin layer of the target material has undergone severe plastic deformations. This explains, at least partially, the observation reported by

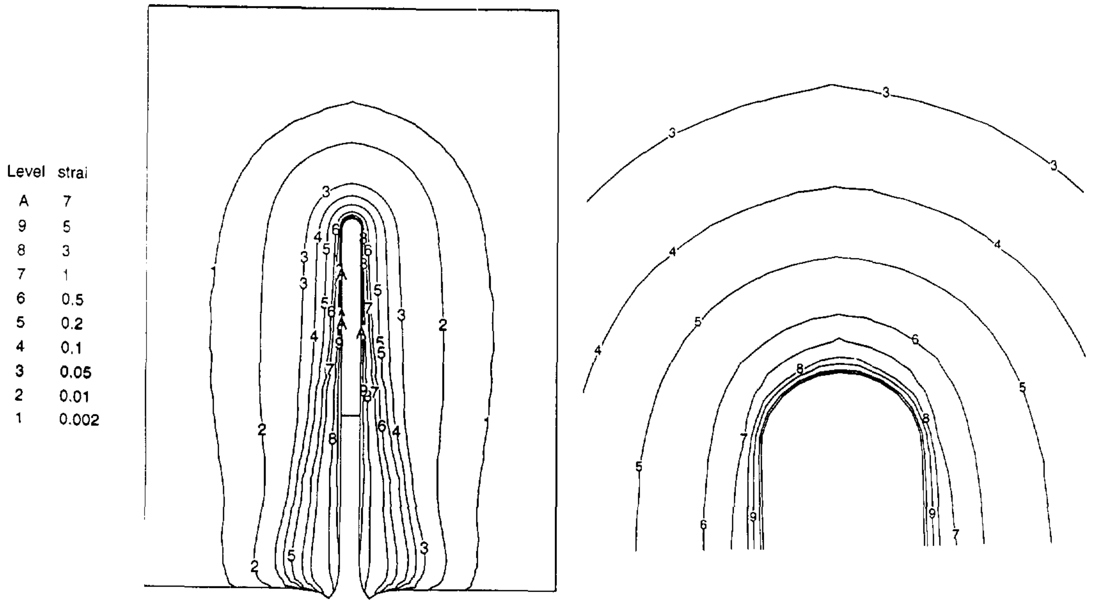

Fig. 8. Contours of the plastic strain in the deforming target region when the penetrator speed equals 39.5% of its initial value of 1.009 km/sec.

Forrestal *et al.* [13] that a thin layer of the target material normal to the target/penetrator interface underwent microstructural changes. From the spacing between the contours of the temperature rise, one can estimate the temperature gradient along the normal to the contours. The temperature gradient, at points on the target/penetrator interface and perpendicular to it, is quite sharp at points in the vicinity of the penetrator nose and drops off significantly as one moves away from the penetrator nose. The time history of the evolution of the temperature of the target particle situated at the penetrator nose tip or the stagnation point, for three different values of the striking speed, is given in Fig. 6(b). The temperature rises sharply in the first few microseconds following the impact and slowly after that because of the lower value of the plastic working needed to deform the material softened by the earlier increase in its temperature. Due to the short duration of the penetration process, the heat lost by conduction is negligible and, because of the high speeds of target particles in the severely deforming region, most of the heat transferred is by convection. As expected, higher striking speeds result in a larger temperature rise of the target particle situated at the nose tip.

The contours of the nondimensional hydrostatic pressure when the penetrator speed equals 0.395 times the initial impact speed of 1009 m/s are plotted in Fig. 7. Peak values, in excess of nine times the yield stress of the target material in a quasistatic simple compression test, of the hydrostatic pressure occur in a small region around the penetrator nose tip. Along

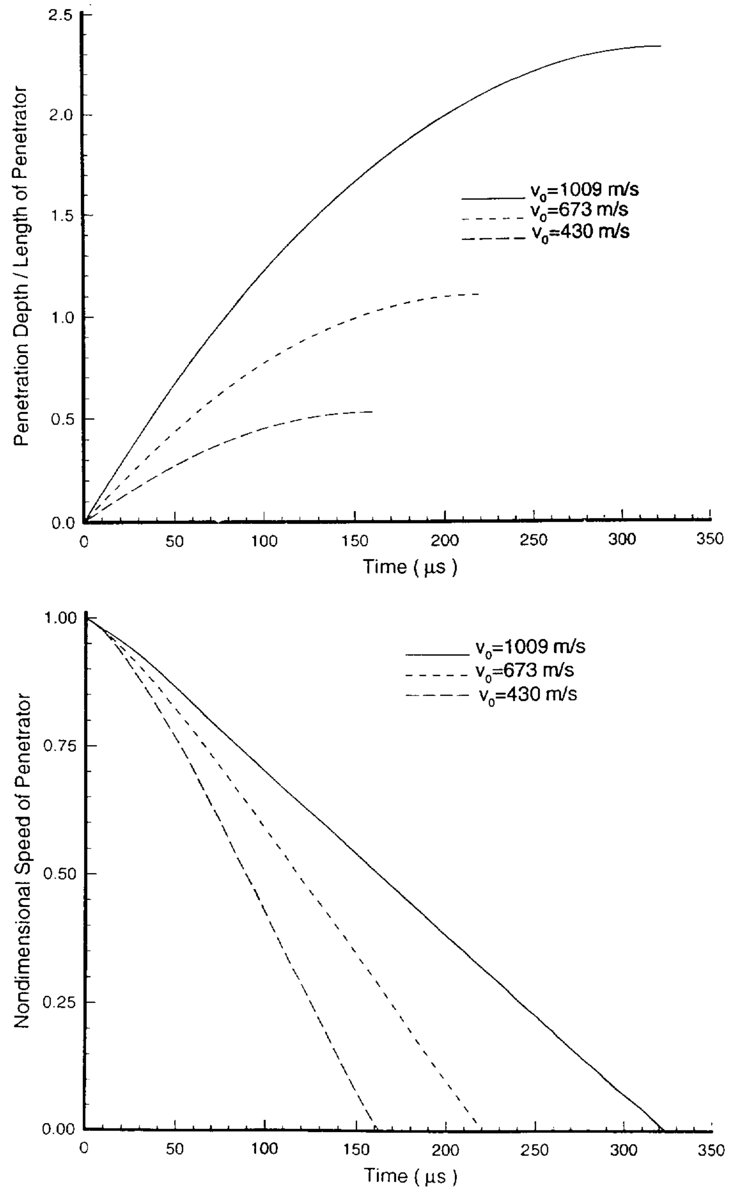

Fig. 9—*Continued opposite.*

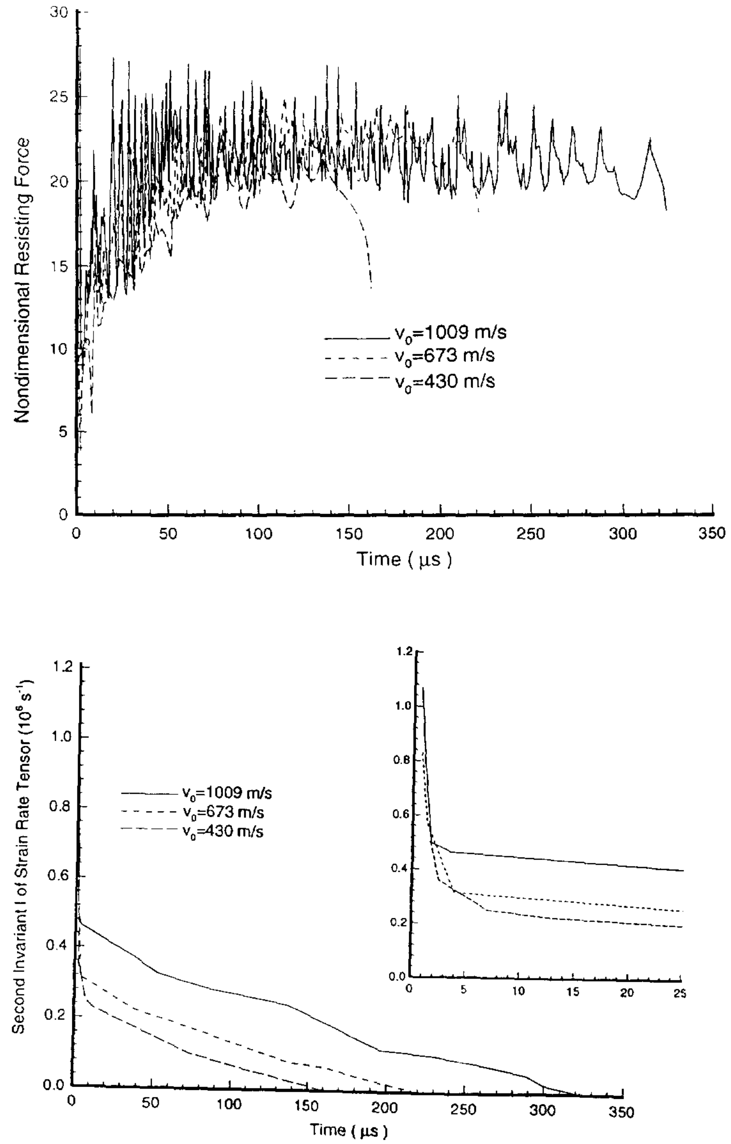

Fig. 9. Histories of the depth of the penetrator nose tip, penetrator speed, resisting force acting on the penetrator and of the second invariant I of the strain-rate tensor at the target particle adjoining the penetrator nose tip for three different values of the striking speed of the penetrator.

any radial line, the pressure drops off rapidly at target particles near the penetrator nose and the rate of drop of the pressure decreases slowly as one moves away from the penetrator nose. For the steady state axisymmetric deformations of a thermoviscoplastic target being penetrated by a rigid ellipsoidal nosed cylindrical rod studied by Batra [22], the peak value of the nondimensional hydrostatic pressure at the penetrator nose tip equalled 11 for $\alpha \equiv \rho v_0^2/\sigma_0 = 1.0$. Batra and Wright [23] found that the axial resisting force experienced by the penetrator and hence p depends weakly upon α. We note that immediately after the impact, the peak hydrostatic pressure near the nose tip exceeded 30 times the yield stress of the target material in a quasistatic simple compression test.

The contours of the internal variable ψ at the instant when the penetrator speed has been reduced to $0.395v_0$ for $v_0 = 1.009$ km/sec plotted in Fig. 8, indicate that more of the target material on the sides of the target/penetrator interface than ahead of it has been severely deformed. We recall that ψ can also be interpreted as the equivalent plastic strain, since its rate of evolution is a linear function of the plastic working. The occurrence of 700% plastic strains at target particles adjacent to the target/penetrator interface lend credence to our assumption of not incorporating elastic shear strains in the problem formulation. It is unlikely that target particles can withstand such high plastic strains without fracturing. Our consideration of the thermal softening of the material accounts at least partially for the loss of the material strength, since severely deformed material particles are also heated up significantly.

The results presented above, except for the history of the evolution of the temperature at the target particle adjoining the penetrator nose tip, are for a fixed value of the striking speed of the penetrator. Figure 9 exhibits histories of the depth of the penetrator nose tip, its speed nondimensionalized with respect to the striking speed, the nondimensional resisting force experienced by the penetrator, and of the second invariant I of the strain-rate tensor at the target particle abutting the penetrator nose tip. The considerably higher values of I during the first microsecond after impact indicate that most severe deformations of the target particle occur during that time and the peak value of I equals 1.1×10^6 s. However, one or so microseconds after the impact, the second invariant I at the target particle adjoining the nose tip drops to nearly one-half of its peak value and then gradually decreases to zero. A plot of the history of the hydrostatic pressure at the stagnation point revealed that the pressure, like the axial resisting force R_t experienced by the penetrator and not shown herein, exhibited oscillatory behavior, the amplitude of the oscillations was somewhat more than that for R_t. In numerical work, these oscillations are usually attributed to the improper choice of the time step size and/or the finite element mesh employed and are sometimes eliminated by introducing artificial viscosity into the problem and/or averaging the consecutive maximum and minimum values and assigning the average value to the midpoint of their time interval. Our reducing Δt to one-half of its value did alleviate the problem somewhat, but the computation time increased enormously. We did not experiment with the introduction of the artificial viscosity since there are dissipative mechanisms due to plastic working and heat conduction included in the problem formu-

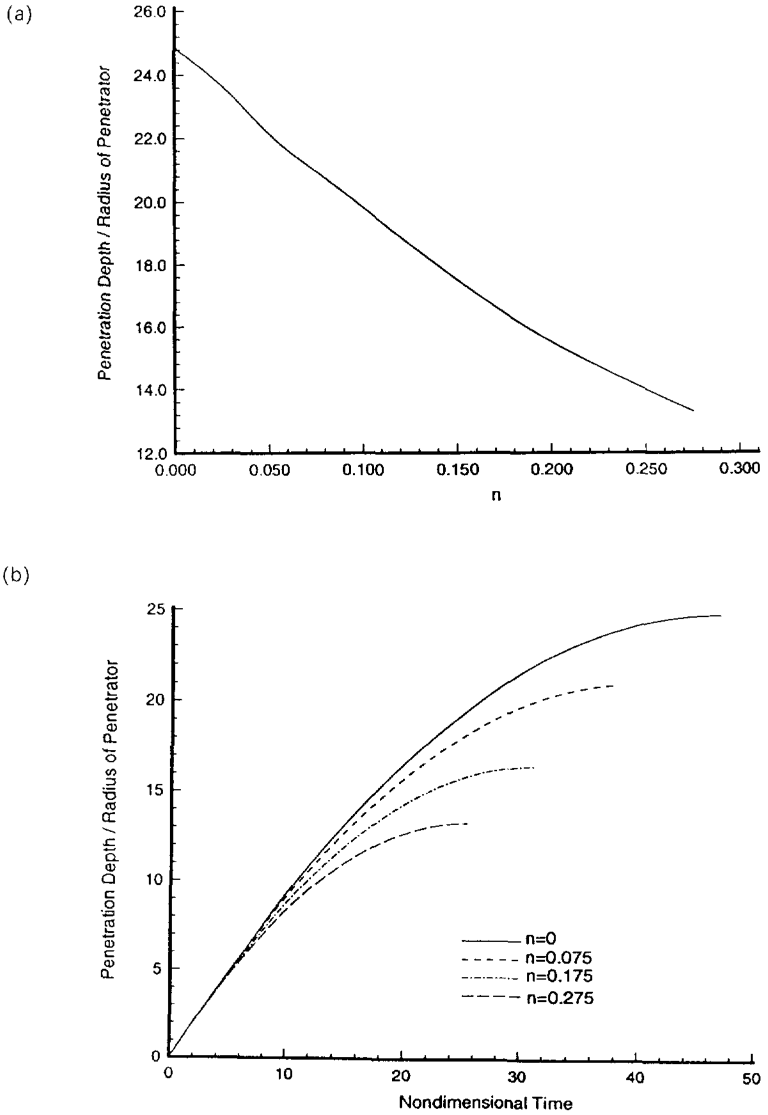

Fig. 10(a) and (b)—*Continued opposite.*

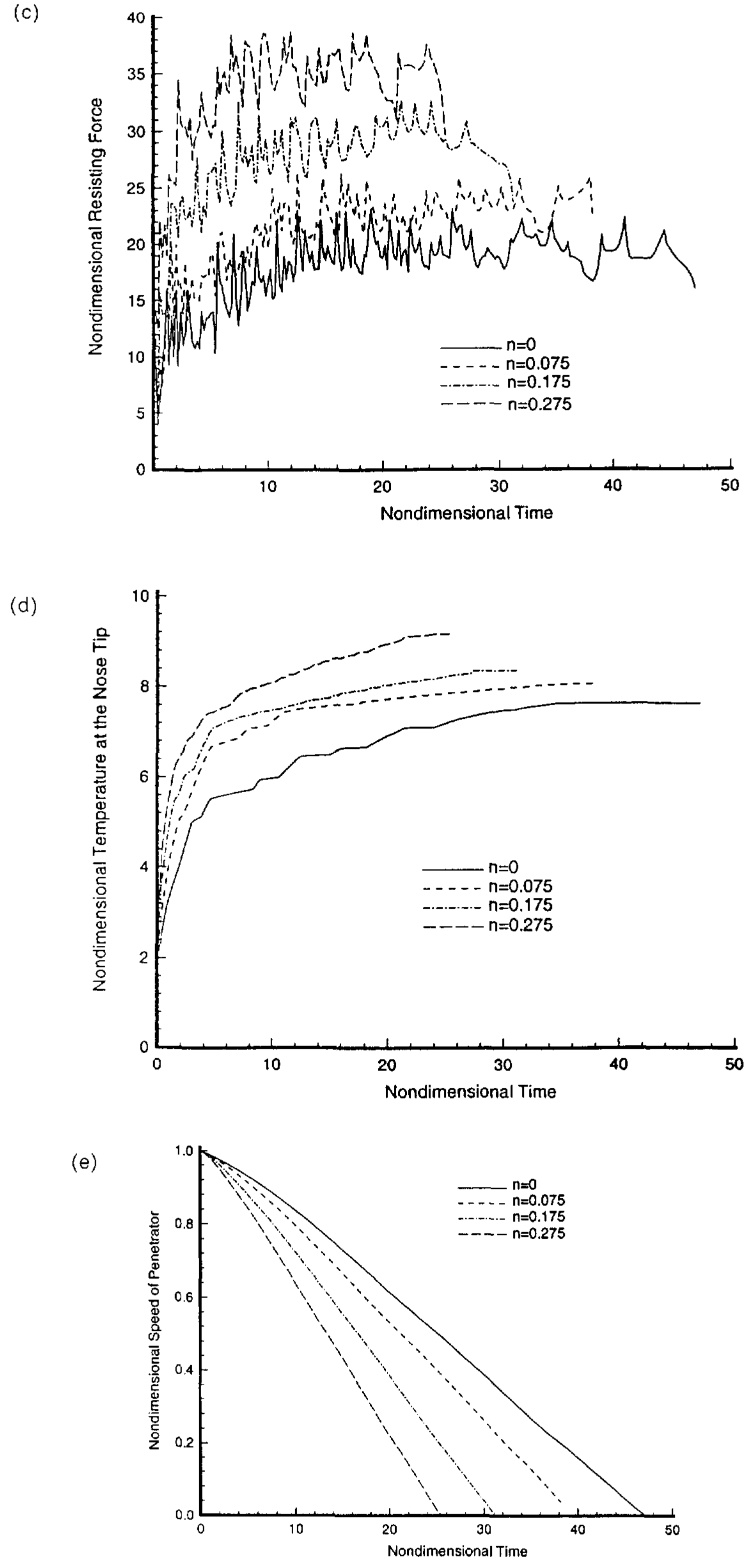

Fig. 10. Effect of the strain-hardening exponent n upon the computed penetration depth and histories of penetrator position, axial resisting force, temperature rise of a target particle adjoining the penetrator nose tip and the penetrator speed.

lation. The averaging technique outlined above does result in a smooth variation of R_t.

The effect of the values of the work-hardening exponent n and the strain-rate hardening exponent m upon the penetration depth, and histories of the distance of the penetrator nose tip from the top surface of the undeformed penetrator, axial resisting force acting on the penetrator, temperature rise of a target particle adjoining the penetrator nose tip, and the speed of the penetrator are depicted in Fig. 10(a)–(e), and Fig. 11(a)–(e), respectively. Results exhibited therein are for a penetrator of mass 23 g impacting the target with a speed of 673 m/sec. We note that values of other parameters were kept fixed when m or n were varied. As expected, higher values of m and n reduce the penetration depth. Higher values of m or n enhance the effective stress required to deform the material plastically at a given value of the plastic strain-rate or plastic strain, respectively, and result in larger values of the axial resisting force acting on the penetrator. It will enhance the incremental plastic work done and heat generated, which will soften the material further. Thus the effect of changing one material parameter manifests itself through varying degrees of change in other effects.

5. CONCLUSIONS

We have studied axisymmetric thermomechanical deformations of a semi-infinite target impacted at normal incidence by a fast-moving, hemispherical nosed, rigid, cylindrical rod. The target material has been presumed to exhibit thermal softening, strain-hardening and strain-rate hardening. The target/penetrator interface has been taken to be smooth and contact conditions thereon have been accounted for by using the slideline algorithm of Hallquist *et al.* [18]. The nonlinear coupled ordinary differential equations, obtained by the Galerkin

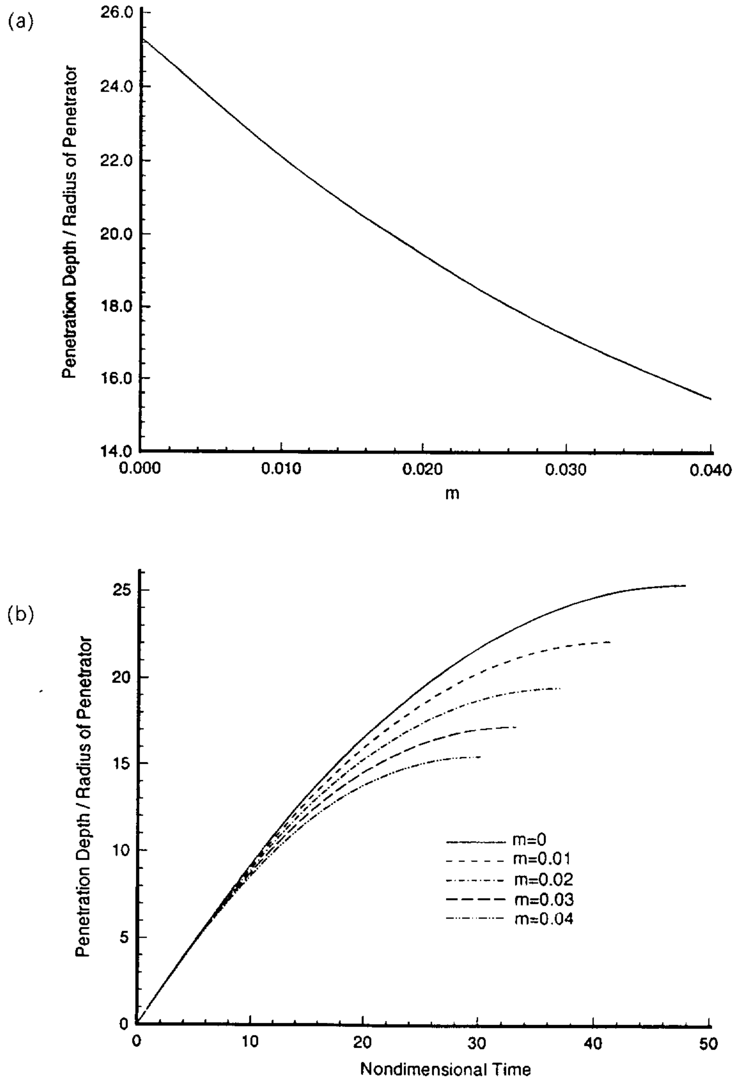

Fig. 11(a) and (b)—*Continued opposite.*

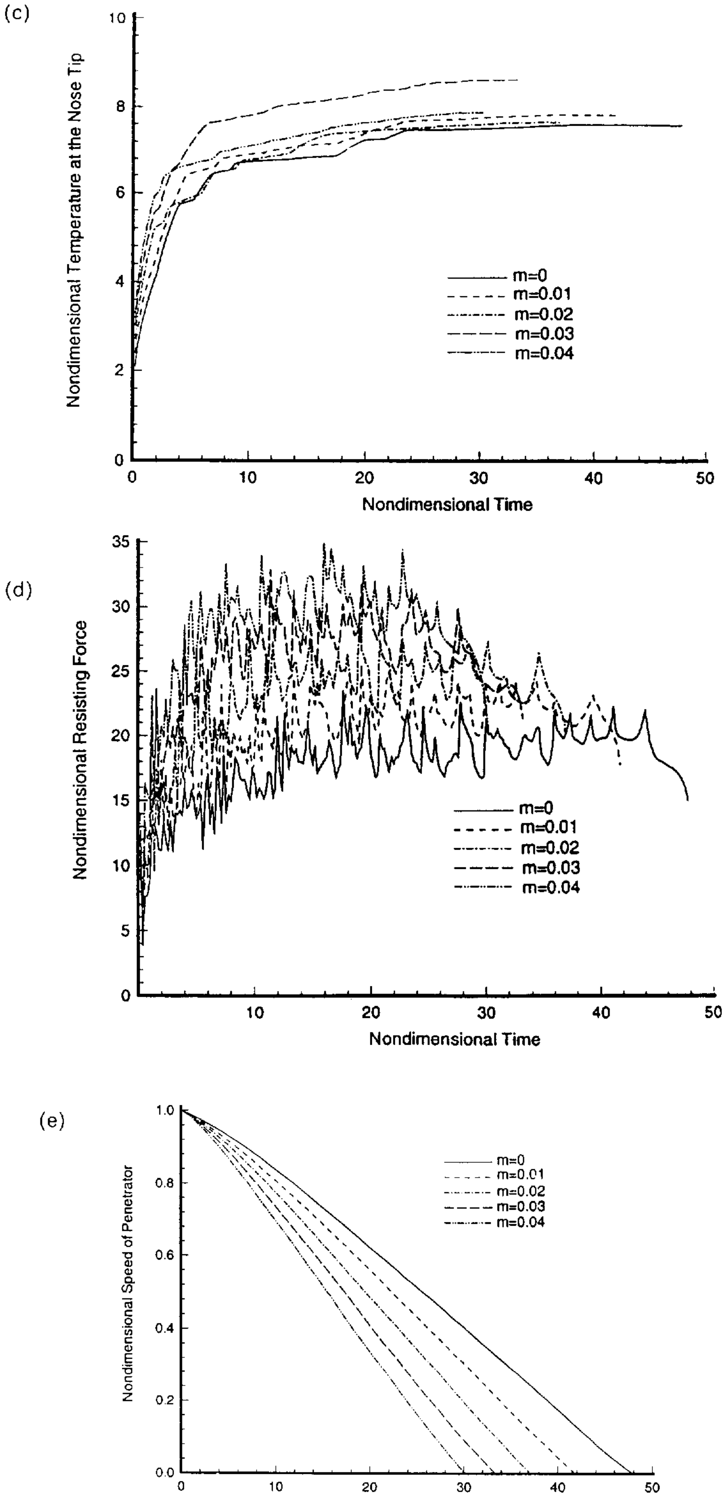

Fig. 11. Effect of the strain-rate hardening exponent m upon the computed penetration depth and histories of penetrator position, axial resisting force, temperature rise of a target particle adjoining the penetrator nose tip and the penetrator speed.

approximation of the partial differential equations governing the thermomechanical deformations of the target material, have been integrated with respect to time t by using the forward difference method.

Sixteen tests involving the penetration of hemispherical nosed steel rods into aluminum targets reported by Forrestal *et al.* [13] have been simulated. The computed penetration depth has been found to correlate very well with the test results for low speeds of impact but exceeds that observed experimentally for high impact speeds. We note that Chen [20], who did not consider thermal softening and strain-rate hardening of the target material but accounted for the frictional force at the target/penetrator interface, under-predicted the penetration depth at higher impact speeds. Both these investigations assumed that material parameters are temperature independent. We found that a thin layer of the target material adjoining the target/penetrator interface melted and the temperature rise at other target particles was also significant. This melted target layer lends credence to the microstructural changes observed by Forrestal *et al.* [13] in the similarly situated target material. Some plausible reasons for the discrepancy between the computed penetration depth and test findings for higher impact speeds have been stated in the text and the effect of each remains to be investigated.

The computed results reveal that plastic deformations of the target material spread further to the sides of the target/penetrator interface than ahead of the penetrator nose. Higher values of the strain hardening exponent and strain-rate hardening exponent reduce the depth of penetration.

Acknowledgements—This work was supported by the U.S. Army Research Office Grant DAAL-03-92-G-0315 to the University of Missouri-Rolla. Some of the computations were performed on the NSF sponsored supercomputer center at the University of Illinois in Urbana.

REFERENCES

1. W. A. Allen and J. W. Rogers, Penetration of a rod into a semi-infinite target. *J. Franklin Inst.* **272,** 284 (1961).
2. D. C. Pack and W. M. Evans, Penetration by high-velocity jets. *Proc. Phys. Soc. London* **B64,** 298–310 (1951).
3. V. P. Alekseevskii, Penetration of a rod into a target at high velocity. In *Combustion, Explosion and Shock Waves*, Vol. 2, pp. 63–66 (translation from Russian). Faraday Press, New York (1966).
4. A. Tate, A theory for the deceleration of long rods after impact. *J. Mech. Phys. Solids* **15,** 387–399 (1967).
5. A. Tate, Further results in the theory of long rod penetration. *J. Mech. Phys. Solids* **17,** 141–150 (1969).
6. T. W. Wright and K. Frank, Approaches to penetration problems. In *Impact: Effects of Fast, Transient Loading* (Edited by W. J. Ammann, W. K. Liu, J. A. Studer and T. Zimmermann). A. A. Balkema, Rotterdam (1988).
7. M. E. Backman and W. Goldsmith, The mechanics of penetration of projectiles into targets. *Int. J. Engng Sci.* **16,** 1–99 (1978).
8. G. H. Jonas and J. A. Zukas, Mechanics of penetration: analysis and experiment. *Int. J. Engng Sci.* **16,** 879–903 (1978).
9. C. E. Anderson and S. R. Bodner, The status of ballistic impact modelling. *Proc. 3rd TACOM Armor Coordinating Conf.*, Feb. 17–19, 1987, Monterey, California.
10. E. W. Billington and A. Tate, *The Physics of Deformation and Flow*. McGraw-Hill, New York (1981).
11. M. Macauley, *Introduction to Impact Engineering*. Chapman and Hall, London (1987).
12. J. A. Zukas (Editor), *High Velocity Impact Dynamics*. John Wiley and Sons, New York (1990).
13. M. J. Forrestal, N. S. Brar and V. K. Luk, Penetration of Strain-hardening targets with rigid spherical-nosed rods. *J. Appl. Mech.* **58,** 7–10 (1991).
14. R. C. Batra and R. Jayachandran, Effect of constitutive models on steady state axisymmetric deformations of thermoelastic-viscoplastic targets. *Int. J. Impact Engng* **12,** 209–226 (1992).
15. S. R. Bodner and Y. Partom, Constitutive equations for elastic-viscoplastic strain-hardening materials. *J. Appl. Mech.* **42,** 385–389 (1975).
16. S. B. Brown, K. H. Kim and L. Anand, An internal variable constitutive model for hot working of metals. *Int. J. Plasticity* **5,** 95–130 (1989).
17. K. J. Bathe, *Finite Element Procedures in Engineering Analysis*. Prentice-Hall, New Jersey (1982).
18. J. O. Hallquist, G. L. Goudreau and D. J. Benson, Sliding interfaces with contact-impact in large-scale Lagrangian computations. *Comput. Meth. Appl. Mech. Engng* **51,** 107–137 (1985).
19. S. L. Semiatin and J. J. Jonas, *Formability and Workability of Metals*. American Society for Metals (1984).
20. E. P. Chen, Finite element simulation of perforation and penetration of aluminum targets by conical-nosed steel rods. *Mech. Mater.* **10,** 107–115 (1990).
21. M. J. Forrestal, Z. Rosenberg, V. K. Luk and S. J. Bless, Perforation of aluminum plates with conical-nosed rods. *J. Appl. Mech.* **54,** 230–232 (1987).
22. R. C. Batra, Steady state penetration of thermoviscoplastic targets. *Comput. Mech.* **3,** 1–12 (1988).
23. R. C. Batra and T. W. Wright, Steady state penetration of rigid perfectly plastic targets. *Int. J. Engng Sci.* **24,** 41–54 (1986).
24. R. C. Batra and K. I. Ko, An adaptive mesh refinement technique for the analysis of shear bands in plane strain compression of a thermoviscoplastic solid. *Comput. Mech.* **10,** 369–379 (1992).